ChemElectroChem

Research Article
doi.org/10.1002/celc.202200102

Chemistry Europe
European Chemical Societies Publishing

www.chemelectrochem.org

Electrodeposition of Cobalt-Copper Oxides Decorated with Conductive Polymer for Supercapacitor Electrodes with High Stability

E. Noormohammadi,[a, b] F. Poli,[b] C. Durante,[c] M. Lunardon,[c] S. Sanjabi,*[a] and F. Soavi*[b]

Here, we report about the synthesis of Cobalt-Copper (CC) mixed oxides prepared by electrodeposition and thermal annealing, and coated with PEDOT:PSS (CCP) for supercapacitor electrodes. The electrodes' morphology and electrochemical performance were investigated by combining XRD, XPS, SEM, cyclic voltammetry, and galvanostatic charge/discharge tests. The initial capacity of the CC electrode was 26 mAh/g at a scan rate of 5 mV/s with a coulombic efficiency of 92%. The CC electrode featured a capacity retention of 81% at a constant current density of 1 A/g after 5000 cycles. CCP electrodes slightly reduced the specific capacity but increased both coulombic efficiency and cyclic stability. CCP1 electrode featured a specific capacity of 21 mAh/g at 5 mV/s scan rate with better coulombic efficiency 95% along with capacity retention of 92.3% over 5000 cycles. Increasing the amount of PEDOT:PSS lowered the CC electrodes' specific capacity, but significantly improved the capacity retention up to 100%.

Introduction

Nowadays, the production and consumption of energy based on the combustion of fossil fuels show a worrying economic and environmental outlook for the world, and it is widely recognized that electrochemical energy storage will be fundamental to allow the widespread use of alternative sources of energy. Electrochemical energy storage and conversion systems include batteries, supercapacitors.[1–2] Supercapacitors possess high power density, long cycle life, high-rate capability, quick charging and discharging, safety, that are qualities that make them ideal for applications in which high powers are required for short time, like memory backups, hybrid-electric vehicles, kinetic recovery systems, power grids stabilization and, electric vehicles.[3–5]

According to the charge storage mechanism of electrode materials, supercapacitors can also be classified into three types: electrical double-layer capacitors (EDLCs), pseudocapacitors (PCs), and battery-like supercapacitors.[6–7] Hybrid supercapacitors combine positive and negative electrodes that are charged by different mechanisms, electrostatic or faradaic. The EDLCs store and release charges in the electric double layer formed at the interface between electrode and electrolyte through a rapid mechanism that makes them suitable for high-power applications.[8] Given the high chemical inertia, electrochemical stability, cost, availability, conductivity, and specific surface area together with the possibility to highly engineer the textural properties of these materials in terms of surface moieties and pores size distributions, carbon-based materials are exploited as the electrode materials for EDLCs.[9–10] PCs electrodes exploit faradaic redox reactions occurring at or near the surface of active materials that often turn into higher specific capacitance with respect to EDLCs. The electrochemical response of PC electrodes is similar to that of EDLC carbons, but their conductivity and cycle life are lower.[11] Battery-type electrode materials store energy by relying on a purely Faradaic process in which electron transfer with slower kinetics than that of PCs materials, that may include phase change during the charge-discharge process occurs. Compared to the pseudocapacitive electrode materials, the battery-type electrode materials show evident reversible redox peaks under cyclic voltammetry (CV), as well as a potential plateau in the galvanostatic charge-discharge (GCD) curve.

Multiple valence states transition metal oxides (TMOs) such as NiO,[12] Co_3O_4 ,[13] $CuCo_2O_4$,[14] and Fe_2O_3[15] have been widely studied as battery-type electrode materials. The spinel structure of transition metal oxides is one of the structures that is attracting much attention for the production of supercapacitors and batteries. Due to the presence of two metals within one molecule, these structures enable to exchange a high number of electrons per mole of oxides. It should also be noted that in many TMOs, the crystal lattices feature well connected and large paths for ion diffusion, and a high surface exposed to the electrolyte.[12–16]

[a] E. Noormohammadi, S. Sanjabi
Nanomaterials group, Department of Materials Engineering
Tarbiat Modares University
14115-143 Tehran, Iran
E-mail: Sanjabi@modares.ac.ir
[b] E. Noormohammadi, F. Poli, F. Soavi
Department of Chemistry "Giacomo Ciamician"
University of Bologna
40126 Bologna, Italy
E-mail: Francesca.soavi@unibo.it
[c] C. Durante, M. Lunardon
Department of Chemical Sciences
University of Padova
35131 Padova, Italy

In recent years, the use of cobalt spinel has been considered as an important class of electroactive materials in energy storage applications. Copper-cobalt spinel ($CuCo_2O_4$), have already been demonstrated to improve energy storage capacity and charging and discharging speed of supercapacitors.[17–19] Generally, $CuCo_2O_4$ has two different crystal structures: the "normal" and the "inverse" spinel structures, represented by the formulas $Cu[Co]_2O_4$ and $Co[CuCo]O_4$, respectively. In addition, $CuCo_2O_4$ usually exhibits higher specific capacity compared with that of single metal oxides such as CuO, Co_3O_4, etc. The reason is that cobalt mainly contributes to the charge storage capacity, while copper enhances the TMO electrical conductivity. Consequently, the activation energy related to the transport of electrons between multiple metal species is reduced. However, in practical applications, $CuCo_2O_4$ still suffers from some drawbacks, for instance, low conductivity, poor cycling stability, and relatively low specific capacity. In order to solve these issues, many efforts have been devoted to the design of spinel $CuCo_2O_4$ electrodes with diverse morphologies.

Several different types of spinel $CuCo_2O_4$ nanostructures have been explored through a variety of synthetic routes comprising electro-spinning, urea combustion method, and hydrothermal.[19] However, the poor cycling stability and the low electrical conductivity are the major drawbacks.[19] Furthermore, the above-mentioned methods require a complex multistep fabrication process that makes the development of $CuCo_2O_4$ nanostructures complicated and costly.[19–21] Therefore, engineering efficient morphologies via a facile and low-cost method is necessary for more advancements in $CuCo_2O_4$ based electrode materials. The use of electrochemical methods to create such structures is very cost-effective. Electrodeposition methods have attracted great interest owing to their advantages such as the easy control of composition, by proper tuning of the process conditions (solution concentration, composition, and electrochemical conditions), the capability to produce structural features with sizes ranging from nm to μm, and the high deposition rate, that in turn is related to lower cost if compared to other multistep synthesis.[20–21] Electrodeposition has generally been found to produce a metastable solid solution when complexing agents are used for the simultaneous co-deposition of cobalt and copper.[20–23]

To improve the overall performance of TMOs-based electrodes, composites, and nanocomposites with conducting polymers, such as polyaniline (PANI), poly(3,4-ethylenedioxythiophene) (PEDOT), polypyrrole (PPy) have been explored.[24–26] One of the most widely investigated conductive polymers is PEDOT due to its high conductivity, transparency, and environmental stability. PEDOT conductivity and solubility can be tuned with the addition of dopants such as the polyelectrolyte poly (styrene sulfonic acid) (PSS) which makes it water-soluble to ease the fabrication process avoiding the exploitation of organic solvents.[27–32]

Compared to PANI or PPy, PEDOT:PSS has the unique advantage of being stable and electronically conductive in the extreme alkaline environment that is needed for the faradaic activity and stability of TMO electrodes. Indeed, according to the Pourbaix diagram, metal oxides are stable at a pH higher than 8, but polymers, like PANI, are electronically conductive only in an acidic environment (protonated form).[33–35] Therefore, the good stability and conductivity of PEDOT:PSS in an alkaline environment, make it a good candidate to bind TMO while simultaneously promoting the electronic connection between TMO particles. In other words, PEDOT:PSS can be exploited as an "active binder" for TMO electrodes. In this work, electrodeposited cobalt-copper oxides on Ni foam (NF) were coated with PEDOT:PSS to prepare composite electrodes tested for supercapacitor applications. $CuCo_2O_4$ was produced by annealing Co–Cu hydroxide films obtained on NF by an electrochemical-chemical process, starting from Cobalt (II) and Copper (II) sulfates in nitric acid. This procedure was previously reported for the preparation of mixed oxides like $NiCoO_2$ and $CuCo_2O_4$.[36–37] Specifically, Co–Cu hydroxides were co-electrodeposited on the NF surface by exploiting the local increase of pH during the cathodic polarization of NF. Indeed, under the cathodic polarization, OH^- is expected to be released at the NF as the product of the reduction of NO_3^- and hydrogen evolution, as for Eqs (1), (2) and, (3). Simultaneously, H_2 bubbles evolved at the NF electrode can drive $CuCo_2O_4$ growth and template the morphology of the oxide layer.[36–40]

$$NO_3^- + 7H_2O + 8e^- \rightarrow NH_4^+ + 10OH^- \quad (1)$$

$$2H^+ + 2e^- \rightarrow H_{2(g)} \quad (2)$$

$$xCu^{2+} + yCo^{2+} + 2(x+y)OH^- \rightarrow Cu_xCo_y(OH)_{2(x+y)} \quad (3)$$

After the electrochemical step, (CuCo) hydroxides were thermally annealed to $CuCo_2O_4$ on the NF substrate as described by eq. (4) for the case in which the Cu-to-Co molar ratio is 1:2.

$$Cu_xCo_{2x}(OH)_{6x} + 1/2xO_2 \rightarrow xCuCo_2O_4 + 3x\ H_2O \quad (4)$$

The structure, composition and oxidation state, and the surface morphology of all the electrodes with and without PEDOT:PSS coating were investigated using XRD, XPS, and SEM, respectively. The electrochemical performance of all prepared electrodes was characterized by cyclic voltammetry (CV), galvanostatic charge/discharge (GCD), and cyclic stability tests.

Experimental Section

Materials

Cobalt (II) sulfate heptahydrate ($CoSO_4 \cdot 7H_2O$) and copper (II) sulfate pentahydrate ($CuSO_4 \cdot 5H_2O$), Nitric acid ($\geq$65%), and PEDOT:PSS were purchased from Sigma Aldrich. Nickel foam was provided from Goodfellow.

Preparation of cobalt-copper oxide (CC) and cobalt-copper oxide/PEDOT:PSS (CCP) coatings

The cobalt-copper oxides (CC) were obtained starting from an aqueous solution containing 0.06 M $CoSO_4 \cdot 7H_2O$ and 0.04 M

$CuSO_4 \cdot 5H_2O$. HNO_3 was added to all solutions to adjust the pH to 1.4. The electrochemical process was run in three electrode-cell, featuring a Ni foam (NF) working electrode, with dimensions of 0.25×0.25 cm^2, a Pt mesh as counter electrode, and Ti grid as reference electrodes, respectively. The Ni foam substrates were cleaned with ethanol in an ultrasonic bath and dried in the atmosphere before electrodeposition. The electrodeposition was carried out at room temperature under galvanostatic conditions with a current density of 1 A/cm^2 for 45 s under solution stirring. The resulting NFs coated with the electrodeposited material were heat-treated at 400 °C for 2 h under unprotected atmosphere. The weight of the oxide electrodeposited on Ni foam substrates was measured by using Mettler Toledo balance and was ca. 3 mg/cm^2. After annealing, the both sides of CC samples were also coated with PEDOT:PSS (0.1 % wt. in aqueous solution, obtained by diluting a Sigma-Aldrich solution with 1.1 % of PEDOT:PSS) by drop casting, followed by drying at 80 °C for one hour. The resulting electrodes are labeled with CCP.

Material characterization

The structure of the electrodeposited coatings was studied using high resolution X-ray diffraction (XRD; PANalytical X'Pert PRO powder diffractometer equipped with a X'Celerator detector CuKα radiation, λ = 1.5406 Å, 40 mA, 40 kV). The composition and the oxidation states of the electrodeposited coatings are characterized by X-ray photoelectron spectroscopy (XPS) surface analysis. The surface morphology, chemical composition, and crystallinity of the samples were examined using scanning electron microscopy (SEM; Zeiss EVO 50 electron scanning microscope (SEM) equipped with an energy-dispersive X-ray analyzer (EDS) from Oxford INCA Energy 350 system.).

Electrochemical characterization

All prepared electrodes have been characterized by cyclic voltammetry (CV), galvanostatic charge/discharge (GCD), and cyclic stability tests. All measurements have been run in 3 M K(OH) electrolyte in a three-electrode cell configuration in which, the prepared electrode was the working electrode, a Pt spring the counter, and Ag/AgCl the reference one, measurements were performed with a (VSP multichannel potentiostat/galvanostat/FRA (BioLogic, Seyssinet-Pariset, France)). CV analysis was performed between −0.2 and 0.45 V (*vs.* Ag/AgCl) at scan rates ranging from 5 to 200 mV/s. Cycling stability was evaluated by GCD tests in a potential window between −0.1 and 0.4 V at a current density of 1 A/g. Electrochemical Impedance Spectroscopy (EIS) was run in the 100 kHz-0.01 Hz frequency range, with 5 mV AC.

Results and Discussion

PEDOT:PSS performance in alkaline electrolyte

At first, the viability of the use of PEDOT:PSS as active binder for cobalt-copper oxides was evaluated by a voltametric study of PEDOT:PSS films coated on NF in 3 M K(OH) electrolyte. Figure 1a) reports 50 CV cycles of PEDOT:PSS at 5 mV/s. The voltammograms show an evident anodic peak at 0.45 V *vs.* Ag/AgCl and a cathodic one at 0.25 V *vs.* Ag/AgCl, indicating that PEDOT:PSS is active, i. e., is doped and undoped in this potential range. In the doped state PEDOT:PSS is electronically conductive. Hence, it can be concluded that PEDOT:PSS can be used as a conductive binder for electrodes working between 0.35 V and 0.45 V *vs.* Ag/AgCl as potential range. Figure 1a) even reports the CV of the bare nickel foam. It indicates that the current collector actively contributes to the cycled capacity with ca. 0.01 mC/cm^2, which corresponds to 30 % of the capacity of the PEDOT:PSS-coated Ni foam (0.035 mC/cm^2). The anodic and cathodic specific capacity, evaluated by the anodic and cathodic peaks, and normalized only to the PEDOT:PSS mass, resulted in 25.7 and 21.6 mAh/g, respectively. The Coulombic efficiency was 84 %, therefore, indicating good reversibility of the doping/undoping process. In addition, the PEDOT:PSS electrode

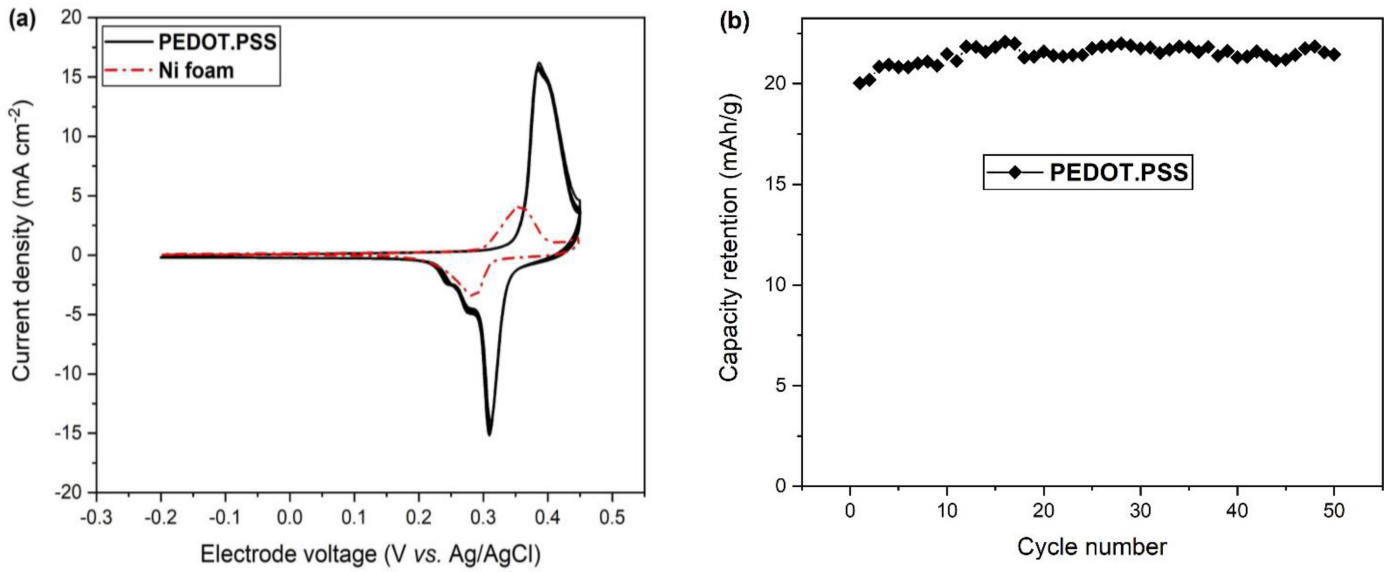

Figure 1. a) 50 CV profiles of PEDOT: PSS-coated nickel foam compared to the CV of the bare current collector and b) trend of the specific capacity of PEDOT-PSS-coated electrode (normalized to the PEDOT:PSS mass)) over cycling, at 5 mV/s in 3 M K(OH).

featured a good capacity retention over 50 cycles as highlighted by the trend reported in Figure 1b), confirming the stability of PEDOT:PSS in an alkaline environment. Therefore, with the aim of improving electrode stability and conductivity, PEDOT:PSS was selected to coat the cobalt-copper oxide layers.

Cobalt-copper oxide electrode preparation

Figure 2 shows the potential profile of the NF working electrode versus time during the galvanostatic step at 1 A/cm^2 adopted for the preparation of CC electrodes. As soon as current flows, the working potential decreases with an instantaneous drop to an extremely negative value, namely below −4 V *vs.* Ag/AgCl. This is a condition that is required to develop a very high local pH by eq (1, 2). Moreover, the potential profile of the working electrodes, reported in Figure 2 is almost constant during the deposition process, a condition that is important to achieve a uniform distribution of the electrodeposited materials and proper coverage of the NF. The cathodic charge, evaluated by the integration of the current over time, resulted in 45 C/cm^2.

After the electrochemical steps, the electrodes were annealed. The resulting electrodes are labeled with CC. Different amounts of PEDOT:PSS were used for the coating of CC electrodes: CCP1, CCP2, and CCP3 featured 0.2, 0.6, and 3.2 mg/cm^2 of polymer, respectively. The composition, the identification code, and the areal mass loading of the prepared and tested electrodes are reported in Table 1.

Structural and morphological analyses

Figure 3 reports the X-ray diffraction pattern of pure cobalt-copper oxide (CC) (black line) and cobalt-copper oxide/0.2 mg.cm^{-2} PEDOT:PSS (CCP1) (red line) electrodes between scattering angles (2θ) of 15° to 80°.

Table 1. Code, composition and areal mass loading of the cobalt-copper oxides without (CC) and with (CCP) PEDOT:PSS.

Name	Composition	Composite mass loading
CC	60%Co oxide – 40%Cu oxide	3.2 ± 0.1 mg cm^{-2}
CCP1	Co–Cu oxide/0.2 mg.cm^{-2} PEDOT:PSS	3.4 ± 0.1 mg cm^{-2}
CCP2	Co–Cu oxide/0.6 mg.cm^{-2} PEDOT:PSS	3.8 ± 0.1 mg cm^{-2}
CCP3	Co–Cu oxide/3.2 mg.cm^{-2} PEDOT:PSS	6.4 ± 0.1 mg cm^{-2}

Both samples display similar XRD diffraction patterns with no difference in the intensity and location of the peaks. As expected, the PEDOT:PSS does not yield any characteristic peak, this could be related to the low load quantity and amorphous nature of the PEDOT:PSS layer. Figure 3 reports three evident peaks indicated by "NF", that are related to the Ni foam substrate. The peaks located at 26°, 31°, 37°, 39°, 59°, and 65° are observed and indexed to the (111), (220), (311), (222), (511) and (440) planes of the spinel cubic $CuCo_2O_4$ phase, respectively (JCPDS card no. 01-1155). The results are in good agreement with previous reports.[41–42]

The surface chemistry of the electrodeposited samples has been investigated by X-ray photoelectron spectroscopy (XPS). Figure 4 reports the composition and the oxidation states of copper, cobalt, and oxygen characterized, the survey analysis of the tested samples (CC & CCP1) is reported in Figure 4a); the main peaks of the target elements (Cu, Co and O) are present for both samples. The Cu $2p_{3/2}$, Co $2p_{3/2}$, and O 1s spectra are shown in Figure 4b), the overlapped peaks are fitted by Gaussian-Lorentzian curves. As expected, CCP1 shows significant contamination of C 1s (from PEDOT:PSS chain). The binding energy (BE) values for the samples calculated from XPS are summarized in Table 2. The Cu 2p and Co 2p spectra were acquired at pass energy of 50 eV for all samples to maximize the transition metal signals, while the O 1s region was acquired at pass energy of 20 eV.

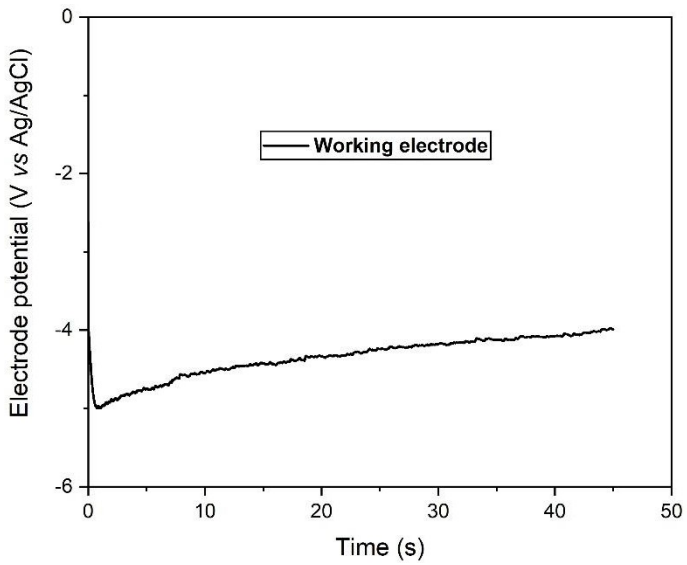

Figure 2. Profile of the NF working electrode during the electrochemical deposition process at 1 A/cm^2.

Research Article
doi.org/10.1002/celc.202200102

Chemistry Europe
European Chemical Societies Publishing

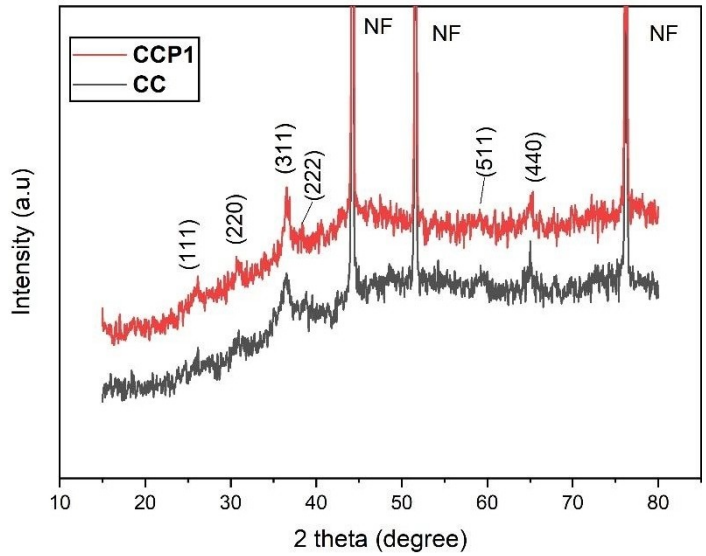

Figure 3. XRD patterns of cobalt-copper oxides (CC) and cobalt-copper oxide/0.2 mg.cm^{-2} PEDOT:PSS (CCP1) electrodes.

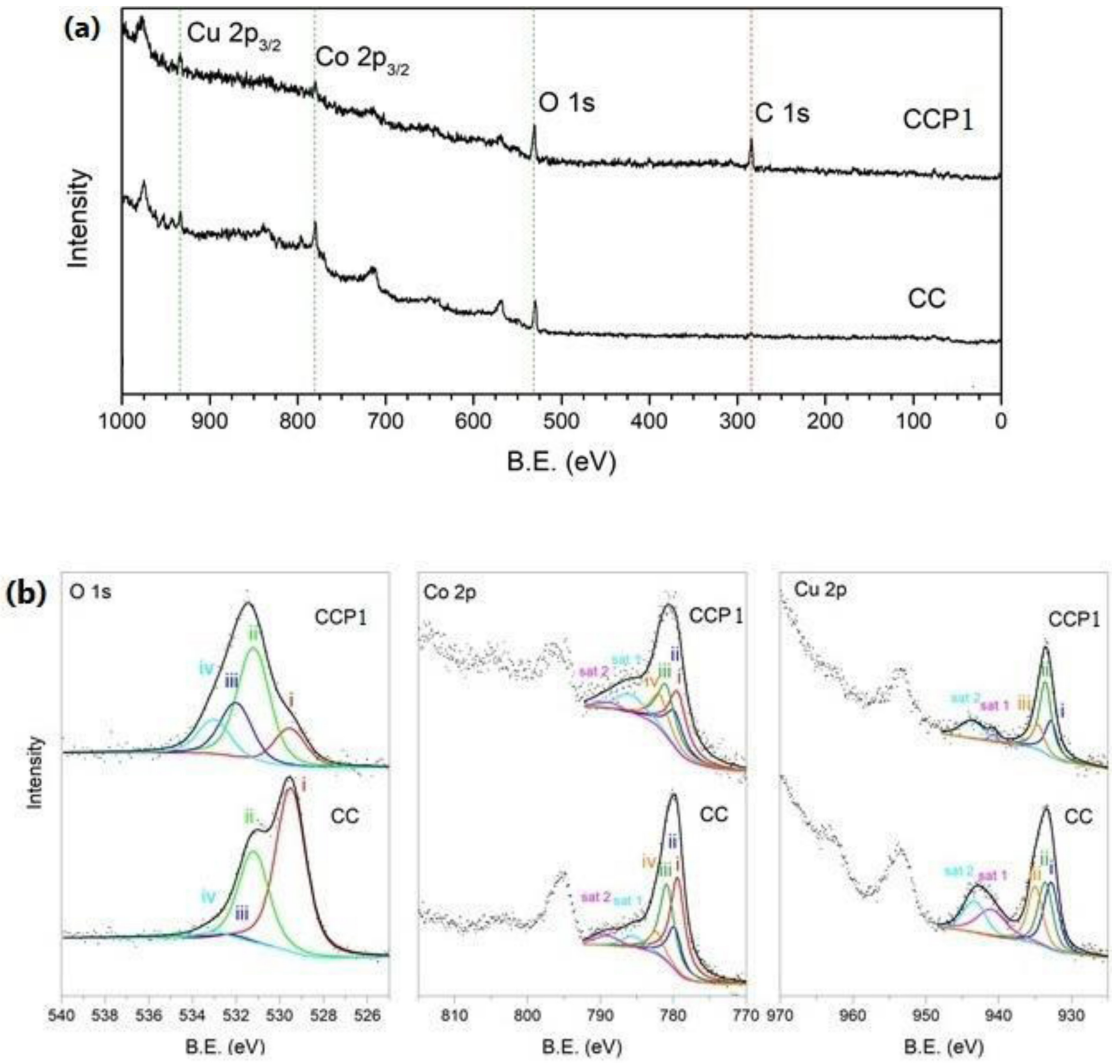

Figure 4. XPS analysis: (a) survey spectrum and (b) XPS spectra of Cu 2p, Co 2p, and O1s of the CC and CCP1 samples.

Table 2. Binding energy (BE) values for the samples calculated from XPS.

Co	Label	CC B.E. [eV]	[%]	CCP1 B.E. [eV]	[%]
Co(III) octahedral	I	779.4	40.1	794.4	32.9
Co(II,III)	Ii	779.8	17.8	779.8	19.8
Co(II) tetraedral	Iii	780.9	32.5	781.0	28.4
Co(II)–OH	Iv	782.3	9.6	781.9	18.9
O					
O^{2-} lattice	I	529.5	61.6	529.6	15.7
O^- or OH^-	Ii	531.2	34.4	531.2	47.1
sub surface O^- species (a)	Iii	532.3	1.7	532.0	22.7
sub surface O^- species (b)	Iv	533.0	2.4	533.0	14.5
water absorption	V				
Cu					
Cu(I) tetrahedral	I	932.8	35.6	932.8	27.3
Cu(II) tetrahedral	Ii	933.6	34.3	933.6	53.9
Cu–OH	Iii	935.0	30.1	934.6	18.8

The core-level analysis of the O1s spectra is performed considering four curve fitting components. The peaks at binding energy (BE) around 529.4–529.6 eV can be attributed to lattice O^{2-} (Cu–O, Co–O); the peaks at BE around 530.5–530.8 eV may be treated as the surface oxygen from a wide variety of species such as adsorbed oxygen O^- and/or OH-like species, as hydroxyl, and carbonate groups; the adjacent peaks at BE around 531.4–531.5 eV and at BE approximately 531.8–532.0 eV, respectively, can be assigned as subsurface O^- species.[43]

The multi-peak analysis of the Cu $2p_{3/2}$ is performed considering five curve fitting components. The peak around 932.8 eV is mostly due to the Cu(I) in a tetrahedral geometry, while the peak around 933.6 eV is due to the Cu(II) in a tetrahedral geometry.[43–45] The presence of the hydroxyl group in O 1s spectra is considered a peak in the 934.5- 935.0 eV region due to the Cu-OH bond.[46] An extra peak in the 931.2–931.4 eV region due to the Cu(I) in an octahedral geometry was considered in the deconvolution process. In the end, two peaks in the 940.3- 941.0 eV and 943.2–943.8 eV regions are considered due to the typical shake-up satellite of Cu 2p.[46]

The multi-peak analysis of the Co $2p_{3/2}$ is performed considering six curve fitting components. The peak around 779.5 eV is mostly due to the Co(III) in an octahedral geometry, while the peak around 781.0 eV is due to the Co(II) in a tetrahedral geometry; the peak in the region of 779.5 −780.0 eV is due to the mixed Co(II), Co(III).[43–45] According to the hydroxyl group presence in O1s spectra, it is considered a peak in the 781.9- 782.3 eV region due to the Co–OH bond. In the end, two peaks in the 788.9- 789.1 eV and 785.5–786.0 eV regions are considered due to the typical shake-up satellite of Co 2p.[47] These results are compatible with the spinel structure and further confirmed the formation of $CuCo_2O_4$ in both CC and CCP1 samples.[43–45]

Figure 5 shows SEM images of the electrodeposited coatings, Figure 5a) depicts a SEM image of the three-dimensional (3D) Ni foam framework. Figure 5b) shows low and high magnification images of the CC structures and it revealed that the cobalt-copper oxide structures are composed of numerous particles sparsely distributed throughout the substrate with a homogeneous size. The particles are interconnected and have grown in the form of cauliflower. Each branch of the cauliflower structure consists of many particles alongside each other. The formation of these porous shaped structures of the electrodeposited cobalt-copper oxide can be related to the hydrogen bubbling on the surface during electrodeposition, which acts as a templating agent. Morphology and structure of PEDOT:PSS is shown in Figure 5c). PEDOT:PSS is deposited completely uniformly on the nickel foam substrate and does not show any preferential growth orientation. Morphology and structure of PEDOT:PSS with cobalt-copper oxides electrode (CCP) is shown in Figure 5d). The PEDOT:PSS has been deposited around the metal oxides and covers the space between the electrodeposited materials which may cause the particles to bond more tightly together and increase their stability and adhesion to the substrate. Figure 5e) shows the distribution of cobalt, copper, and oxygen elements by EDS mapping in CCP sample marked in red, green, and blue, respectively. EDX mapping by SEM (Figure 5e)) indicates that the sample contains a larger amount of cobalt oxygen, and copper this was expected due to the percentage of precursor in the solution (60% $CoSO_4$ and 40% $CuSO_4$) used for electrodeposition. On the other hand, based on the atomic percentage of elements in the coating, the existence of cobalt-copper spinel structure is very likely, and it can be achieved by co-electrodeposition. The concentration of elements in both samples which is taken by EDS of SEM can be observed in Figure 5e).

Electrochemical characterization

The performance of the prepared electrode CC and CCP was evaluated in 3 M K(OH) by CV and galvanostatic charge/discharge, the results of these tests are reported in Figure 6. CV tests were performed to investigate the occurrence of reversible faradaic reaction at the electrode and a suitable potential range where high coulombic efficiency could be achieved. Figure 6a) shows the cyclic voltammogram curves (CV) for CC electrodes at different scan rates ranging from 5 mV/s to 200 mV/s. The highest coulombic efficiencies, of 92% and 95%, for CC and CCP, were achieved in the potential range of −0.1 to 0.4 V *vs.* Ag/AgCl. In the cathodic scan, the CV curves of CC exhibited well-defined redox peaks which is a characteristic of battery-like electrodes at 0.35 and 0.28 V *vs.* Ag/AgCl. The redox peaks correspond to the reversible reactions of the couples Co^{3+}/Co^{2+} and $Cu2^{+}/Cu^{+}$ associated with the presence of OH^- from the K(OH) electrolyte. The redox reactions in an alkaline medium are described by the equations (5)-(7):[48]

$$CuCo_2O_4 + H_2O + e^- \leftrightarrow 2CoOOH^- + Cu(OH)^+ \quad (5)$$

$$CoOOH^- + OH^- \leftrightarrow CoO_2 + H_2O + 2e^- \quad (6)$$

$$Cu(OH)^+ + e^- \leftrightarrow Cu(OH) \quad (7)$$

The shape of the CV curves was not significantly influenced by increasing scan rates, implying reversibility of redox reaction

Research Article
doi.org/10.1002/celc.202200102

Chemistry Europe
European Chemical Societies Publishing

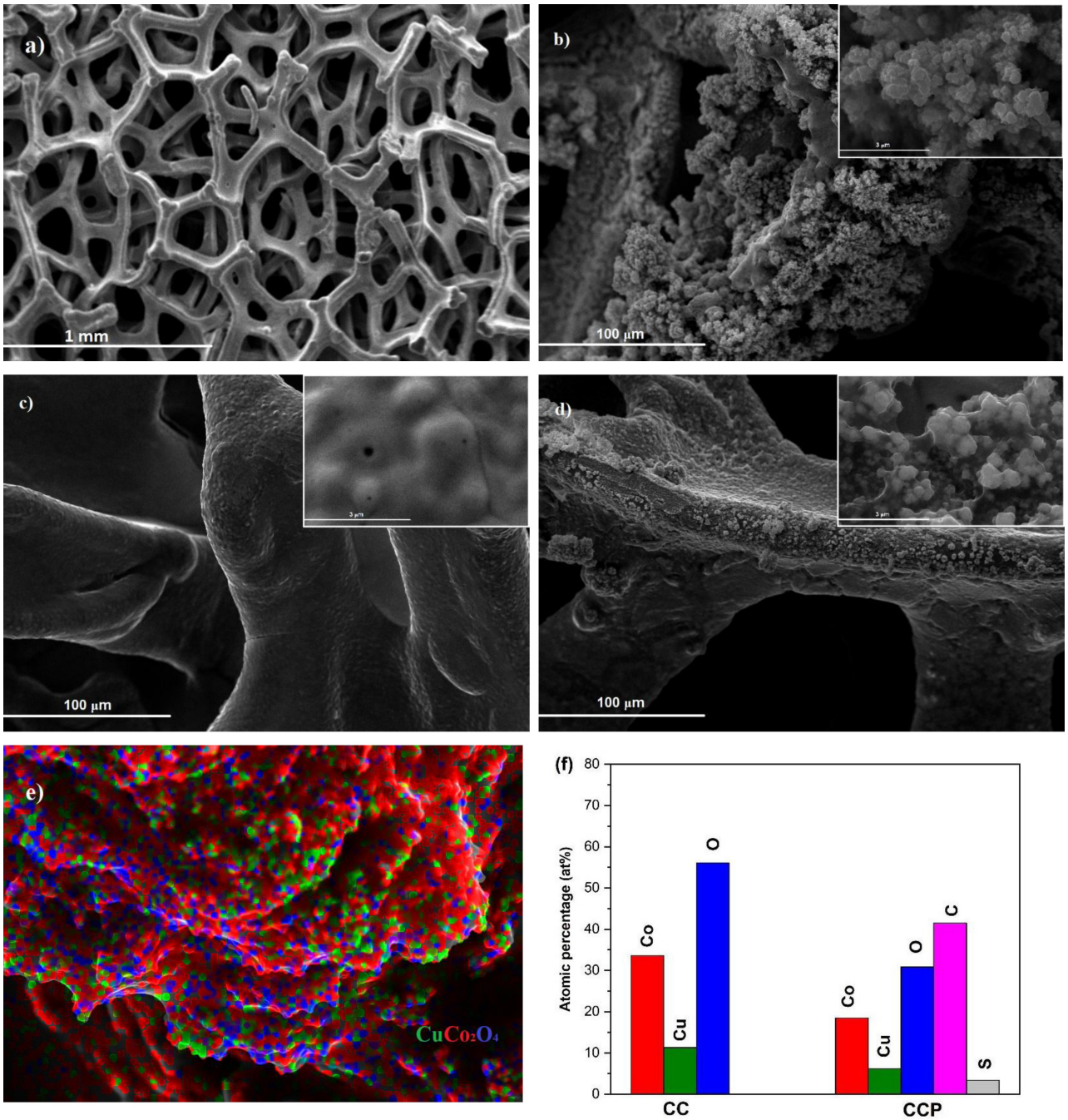

Figure 5. SEM images for (a) nickel foam, (b) CC electrode, (c) PEDOT:PSS, (d) CCP1 electrode; (e) EDX mapping for CC electrode and (f) elements composition in both samples using EDS.

and good power property. However, increasing the scan rate, the anodic and cathodic peaks shifted towards higher and lower potential, respectively. This was due to electrode over-potentials including slow kinetics of electrolyte ion transport in the active layer at high scan rates.[6]

Notably, the CC faradaic processes take place in a potential range that overlap with the PEDOT:PSS ones (Figure 1a) and 6a)), therefore suggesting the viability of the use of PEDOT:PSS as active binder.

Hence, different amounts of PEDOT:PSS, specifically 0.2 (CCP1), 0.6 (CCP2) and 3.2 (CCP3) mg/cm^2 were coated on CC electrode, and then all PEDOT:PSS-coated electrodes (CCP) were tested in the same condition than CC.

Figure 6b) compares CV profiles of CC and CCP1 electrodes at 5 mV/s. The CV response of the two electrodes is similar, therefore suggesting that presence of PEDOT:PSS does not affect the mixed-oxide faradaic reactions.

Electrodes exhibiting redox peaks in CV should not be interpreted as pseudocapacitive as the capacitance of the

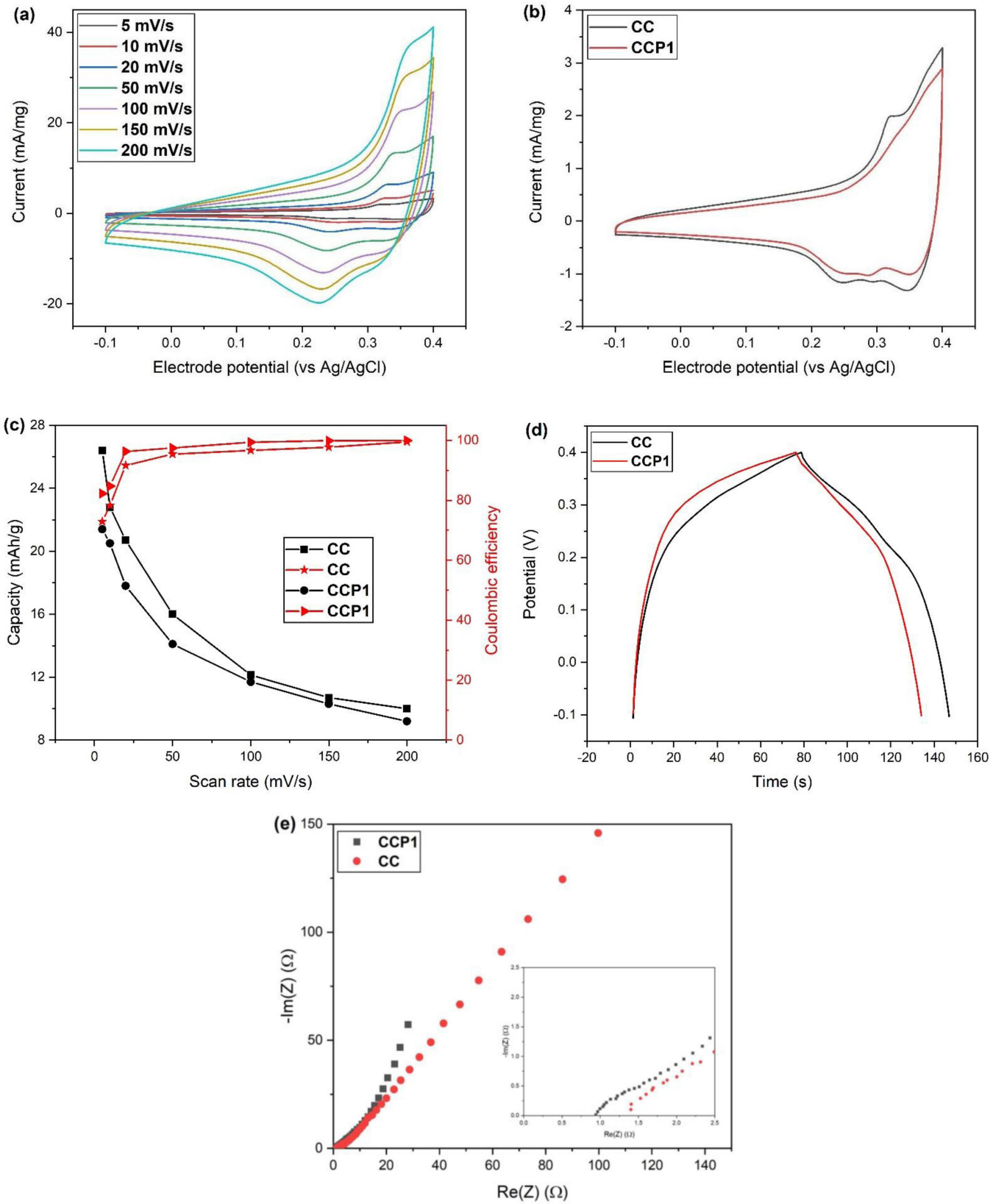

Figure 6. (a) CV s of CC electrode at different scan rates, (b) comparison of the CVs of CC and CCP1 electrodes at 5 mV/s, (c) CV capacity and coulombic efficiency of CC and CCP1 electrodes at different scan rates, and (d) GCPL profiles at 1 A/g and (e) Nyquist plots of CC and CCP1 electrodes (the inset is the magnification at the highest frequencies). Specific current and capacity are calculated considering all the composite layer (oxides and PEDOT:PSS).

electrode keeps on changing over the whole potential window. Therefore, the electrochemical performance of CC and CCP1 was evaluated in terms of specific capacity Qs (mAh/g).[8] The specific capacity was calculated from the integral of the CV cathodic current over time, using Eq. (8).

$$Q_s = \frac{1}{3.6\ m}\int_{t_i}^{t_f} I \times t\ dt \quad (8)$$

where m is the mass of the composite material, including PEDOT:PSS. The calculated specific capacity values for CC and CCP1 were found to be 26 and 22 mAh/g, respectively at 5 mV/s. The presence of the PEDOT:PSS slightly lowers Qs which can be explained with a barrier effect of the polymer that reduces the oxides surface exposed to the electrolyte.

Figure 6c) reports the values of Qs and coulombic efficiency of the electrodes at different scan rates. By increasing the scan rate, the capacity of both electrodes decreases with almost the same rate, but CCP1 features higher coulombic efficiency. The capacity of CC electrode lowers from 26 mAh/g at 5 mV/s to 10 mAh/g at 200 mV/s implying a 62% decrease in capacity. For CCP1, at 5 and 200 mV/s Qs is 22 and 9 mAh/g, which represents a decrease of 59%. If only the oxide mass is considered, then Qs of CCP1 results in 23.4 mAh/g and 9.4 mAh/g at 5 and 200 mV/s, that well compare with the values obtained with CC.

Figure 6d), shows the galvanostatic charge/discharge curves of CC and CCP1 electrodes at 1 A/g with a potential range of −0.1 to 0.4 V. Under GCD, the electrode potential profile, showed significant deviation from linear discharge curves, confirming that the tested material behaves as a Faradaic one. The specific capacity of the electrodes was calculated from the galvanostatic discharge curves using Eq. (9):

$$Q_s = \frac{I \times \Delta t}{m} \quad (9)$$

where I is the current (A), m is the mass loading of the oxide and PEDOT:PSS (composite) on the electrode (g) and Δt is the discharge time (s). At 1 A/g Qs was 26 and 22 mAh/g for CC and CCP1, respectively. It is worth mentioning that these values are calculated considering only the active materials. However, as shown by Figure 1a), if the Nickel foam is not perfectly coated with the oxides and partially exposed to the electrolyte, even the current collector could contribute to the cycled capacity.

In the potential range 0.4–0.2 V *vs.* Ag/AgCl the electrode potential linearly changes with the charge. Therefore, it can be claimed that only within this range the electrodes feature a pseudocapacitive behavior. From the slope of the discharge curve, a capacitance of 280 F/g for CC and 265 F/g for CCP was evaluated.

Figure 6e) compares the Nyquist plots of the CC and CCP1 electrodes. The figure inset is the magnification of the plots at the highest frequencies. The high-frequency intercept with the real axis corresponds to the uncompensated resistance, that includes the electrode electronic resistance and the electrolyte ionic resistance, which in turn depends on cell geometry (distance of the working electrode from the reference). CCP1 features a high-frequency resistance of 0.94 ohm that is lower than that of CC (1.4 ohm). Given that the two measurements were carried out using the same electrolyte and cell set up, we can argue that the lower resistance of CCP1 is related to its better conductivity achieved by PEDOT:PSS coating. In addition, the low-frequency impedance of CC corresponds to a Warburg transmission line that is typical of processes limited by the electron and/or ion diffusion through the electrode.[49] In CCP1, the transmission line is shorter than in CC, presumably because PEDOT:PSS improves electron mobility through the CuCo oxide particles.

To investigate the stability of the electrodes, GCD charge/discharge cycles were performed for 5000 cycles at 1 A/g current density. Figure 7 compares the trends of Qs over cycling and the corresponding capacity retention of all electrodes, including those featuring higher loading of PEDOT:PSS. To better highlight the effect of PEDOT:PSS coating, CCP2 and CCP3 electrodes with increased content of PEDOT:PSS, i.e., 0.6 mg/cm^2 and 3.2 mg/cm^2, were also tested. Increasing the amount of PEDOT:PSS improves the cyclic stability of the electrode, but it simultaneously decreases Qs. Indeed, electrodes containing PEDOT:PSS exhibited a capacity retention that increased with the amount of PEDOT:PSS, from 92% of CCP1 up to 96% with CP2 and 100% for CCP3. Instead, CC retained only 81% of its initial capacity after 5000 cycles. Table 3 compares our results with the cycling performance of cobalt-copper-based electrodes, already reported in literature. It highlights the beneficial effect of the use of PEDOT:PSS on cycle-life.

However, the specific capacity of CCP2 and CCP3 was lower than those of CC and CCP1 and resulted in 15.9 and 11.6 mAh/g, respectively. If specific capacity is normalized only considering the oxides, then Qs becomes 23.4 mAh/g, 18.9 mAh/g and 23.2 mAh/g for CCP1, CCP2 and CCP3, respectively. Overall, these results confirmed that PEDOT:PSS acts as a binder leading to higher cyclic stability and more capacity retention. However, for its low OH^- permeability, it might also act as a barrier *vs.* the

Table 3. Cycling performance of cobalt-copper-based electrodes.

Material	Current density	Capacity retention	Cycle number	Ref
$CuCo_2O_4$ nanosheets/Graphite paper	1 A/g	79.7%	5000	[50]
Chrysanthemum-like $CuCo_2O_4$	0.5 A/g	85%	2000	[51]
Chestnut-like $CuCo_2O_4$/NF	1 A/g	85.2%	5000	[52]
Flower-like $CuCo_2O_4$	2 A/g	86.3%	5000	[53]
Cedar leaf-like $CuCo_2O_4$/NF	1.08 A/g	88%	2000	[54]
$CuCo_2O_4$ nanosheets/NF	1 A/g	90%	5000	[55]
Our work	1 A/g	>92.3%	5000	–

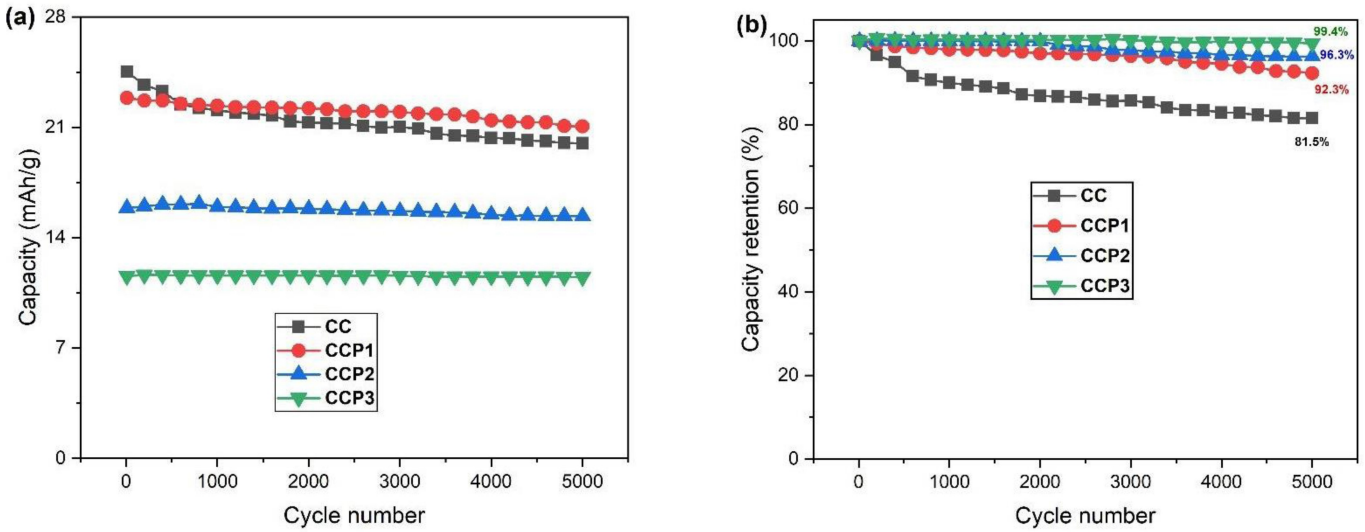

Figure 7. (a) Trend of the capacity over cycling at 1 A/g and (b) capacity retention of CC and CCP electrodes. Specific current and capacity are calculated considering all the composite layer (oxides and PEDOT:PSS).

electrolyte and in part limit the exploitation of the active material.

Conclusion

In summary, the $CuCo_2O_4$(CC)@ PEDOT:PSS (CCP) composites were prepared on nickel foam by electrochemical deposition by inducing a local pH variation, and exploiting H_2 bubbles as templating agents. Electrode coating with PEDOT:PSS is a simple approach to improve the cycling performance of CoCu based electrodes. Indeed, commercial aqueous solutions of PEDOT:PSS are readily available and easy to be used by casting and drying in the ambient atmosphere and at moderate temperatures. X-ray diffraction showed the presence of cobalt-copper oxide spinel structure and no change in the structure of oxides due to the addition of PEDOT:PSS. The initial capacity of the CC electrode was 26 mAh/g at a scan rate of 5 mV/s with a coulombic efficiency of 92%. Also, it showed a capacity retention of 81% at a constant current density of 1 A/g after 5000 cycles. The presence of PEDOT:PSS in the coatings reduced the capacity and increased the cyclic stability of CC electrodes. CCP1 electrode capacity was 21 mAh/g at 5 mV/s scan rate with better coulombic efficiency than CC electrode (95%), and capacity retention of 92.3% over 5000 galvanostatic cycles. Increasing PEDOT:PSS lowered CC electrode capacity, but significantly improved the cyclic stability and capacity retention after 5000 cycles up to 100%. Overall, this study demonstrates that PEDOT:PSS can be a valuable candidate to enhance electrode stability of Co–Cu mixed oxides. Future work will focus on improving the inherent specific capacity of the oxide by improving morphology and surface area and or tuning the Co–to-Cu ratio.

Acknowledgements

The work was funded by Alma Mater Studiorum-Università di Bologna (RFO, Ricerca Fondamentale Orientata) Open Access Funding provided by Universita degli Studi di Bologna within the CRUI-CARE Agreement.

Conflict of Interest

The authors declare no conflict of interest.

Data Availability Statement

The data that support the findings of this study are available from the corresponding author upon reasonable request.

Keywords: Cobalt-copper oxides · Conductive polymer · Cycling stability · Electrodeposition · PEDOT:PSS · Supercapacitor electrode

[1] M. Winter, R. J. Brodd, *Chem. Rev.* **2004**, *104*, 4245–4269.
[2] H. Lund, *Energy* **2007**, *32*, 912–919.
[3] M. S. Whittingham, R. F. Savinell, T. Zawodzinski, *Chem. Rev.* **2004**, *104*, 4243–4244.
[4] M. Kim, J. Kim, *Phys. Chem. Chem. Phys.* **2014**, *16*, 11323.
[5] Y. Zhai, Y. Dou, D. Zhao, P. F. Fulvio, R. T. Mayes, S. Dai, *Adv. Mater.* **2011**, *23*, 4828–4850.
[6] B. Dunn, H. Kamath, J. M. Tarascon, *Science* **2011**, *334*, 928.
[7] T. Wang, H. Chen, F. Yu, X. Zhao, H. Wang, *Energy Storage Mater.* **2019**, *16*, 545–573.
[8] Y. Gogotsi, R. M. Penner, *ACS Nano* **2018**,12, 2081–2083.
[9] A. C. Forse, C. Merlet, J. M. Griffin, C. P. Grey, *J. Am. Chem. Soc.* **2016**, *138*, 5731–5744.
[10] L. Wen, F. Li, H. M. Cheng, *Adv. Mater.* **2016**, *28*, 4306–4337.

[11] Q. Wang, J. Yan, Z. Fan, *Energy Environ. Sci.* **2016**, *9*, 729–762.
[12] M. R. Lukatskaya, S. Kota, Z. Lin, M. Q. Zhao, N. Shpigel, M. D. Levi, J. Halim, P. L. Taberna, M. W. Barsoum, P. Simon, Y. Gogotsi, *Nat. Energy* **2017**, *2*, 17105.
[13] S. C. Sekhar, G. Nagaraju, J. S. Yu, *Nano Energy* **2018**, *48*, 81–92.
[14] Y. Xu, Z. Liu, D. Chen, Y. Song, R. Wang, *Prog. Nat. Sci.* **2017**, *27*, 197–202.
[15] A. Pendashteh, S. E. Moosavifard, M. S. Rahmanifar, Y. Wang, M. F. El-Kady, R. B. Kaner, M. F. Mousavi, *Chem. Mater.* **2015**, *27*, 3919–3926.
[16] V. D. Nithya, N. S. Arul, *J. Power Sources* **2016**, *327*, 297–318.
[17] S. Vijayakumar, S. H. Lee, K. S. Ryu, *Electrochim. Acta.* **2015**, *182*, 979–986.
[18] S. K. Kaverlavani, S. E. Moosavifard, A. Bakouei, *J. Mater. Chem. A.* **2017**, *5*, 14301–14309.
[19] J. Sun, C. Xu, H. Chen, *J. Mater.* **2021**, *7*, 98–126.
[20] E. Gomez, A. Labarta, A. Llorente, E. Valles, *J. Electroanal. Chem.* **2001**, *517*, 63–68.
[21] E. Gomez, A. Llorente, X. Alcobe, E. Valles, *J. Solid State Electrochem.* **2004**, *8*, 82–88.
[22] H. J. Blythe, V. M. Fedosyuk, *J. Magn. Magn. Mater.* **1996**, *155*, 352–354.
[23] V. M. Fedosyuk, O. I. Kasyutich, D. Ravinder, H. J. Blythe, *J. Magn. Magn. Mater.* **1996**, *156*, 345–346.
[24] Q. Wu, Y. Xu, Z. Yao, A. Liu, G. Shi, *ACS Nano* **2010**, *4*, 1963–1970.
[25] G. A. Snook, P. Kao, A. S. Best, *J. Power Sources* **2011**, *196*, 1–12.
[26] Z. Su, C. Yang, C. Xu, H. Wu, Z. Zhang, T. Liu, C. Zhang, Q. Yang, B. Li, F. Kang, *J. Mater. Chem. A.* **2013**, *1*, 12432–12440.
[27] G. Greczynski, T. Kugler, W. R. Salaneck, *Thin Solid Films* **1999**, *354*, 129–135.
[28] J. Ouyang, Q. Xu, C. W. Chu, Y. Yang, G. Li, J. Shinar, *Polymer* **2004**, *45*, 844–850.
[29] X. Crispin, F. L. E. Jakobsson, A. Crispin, P. C. M. Grim, P. Andersson, A. Volodin, C. Haesendonck, M. V. Auweraer, W. R. Salaneck, M. Berggren, *Chem. Mater.* **2006**, *18*, 4354–4360.
[30] A. M. Nardes, M. Kemerink, M. M. Kok, E. Vinken, K. Maturova, R. A. J. Janssen, *Org. Electron.* **2008**, *9*, 727–34.
[31] Y. Hou, Y. Cheng, T. Hobson, J. Liu, *Nano Lett.* **2010**, *10*, 2727–2733.
[32] G. Cai, P. Darmawan, M. Cui, J. Wang, J. Chen, S. Magdassi, P. S. Lee, *Adv. Energy Mater.* **2016**, *6*, 1501882.
[33] Y. Mochizuki, T. Horii, H. Okuzaki, *Trans. Mater. Res. Soc. Jpn.* **2012**, *37*, 307–310.
[34] S. Kim, S. Y. Kim, M. H. Chung, J. Kim, J. H. Kim, *J. Mater. Chem. C.* **2015**, *3*, 5859–5868.
[35] K. Sun, S. Zhang, P. Li, Y. Xia, X. Zhang, D. Du, F. H. Isikgor, J. Ouyang, *J. Mater. Sci. Mater. Electron.* **2015**, *26*, 4438–4462.
[36] L. Abbasi, M. Arvand, *Appl. Surf. Sci.* **2018**, *445*, 272–280.
[37] C. Yuan, J. Li, L. Hou, X. Zhang, L. Shen, X. W. Lou, *Adv. Funct. Mater.* **2012**, *22*, 4592–4597.
[38] S. Vesztergom, A. Dutta, M. Rahaman, K. Kiran, I. Z. Montiel, P. Broekmann, *ChemCatChem* **2021**, *13*, 1039–1058.
[39] A. Sukeri, E. J. C. Junior, M. Bertotti, *Electrochem. Commun.* **2019**, *100* 96–99.
[40] Z. Chen, X. Yan, M. Xu, K. Cao, H. Zhu, L. Li, J. Duan, *ACS Appl. Mater. Interfaces.* **2017**, *9*, 30617–30625.
[41] Y. Sharma, N. Sharma, G. V. S. Rao, B. V. R. Chowdari, *J. Power Sources* **2007**, *173*, 495–501.
[42] A. Pendashteh, M. S. Rahmanifar, R. B. Kaner, M. F. Mousavi, *Chem. Commun.* **2014**, *50*, 1972.
[43] A. Amri, X. F. Duan, C. Y. Yin, Z. T. Jiang, M. M. Rahman, T. Pryor, *Appl. Surf. Sci.* **2013**, *275*, 127–135.
[44] J. Yang, H. Liu, W. N. Martens, R. L. Frost, *J. Phys. Chem. C.* **2010**, *114*, 111–119.
[45] N. C. D. Nath, T. Debnath, E. K. Kim, M. A. A. Shaikh, J. J. Lee, *Electrochim. Acta* **2018**, *273*, 474–482.
[46] M. C. Biesinger, *Surf. Interface Anal.* **2017**, *49*, 1325–1334.
[47] M. C. Biesinger, B. P. Payne, A. P. Grosvenor, L. W. M. Lau, A. R. Gerson, R. S. C. Smart, *Appl. Surf. Sci.* **2011**, *257*, 2717–2730.
[48] L. Zhang, R. Li, W. Li, R. Li, C. Li, Y. Zhou, *RSC Adv.* **2020**, *10*, 22775–22782.
[49] T. Q. Nguyen, C. Breitkopf, *J. Electrochem. Soc.* **2018**, *165*, 826–831.
[50] S. Liu, K. S. O. Hui, K. N. Hui, *ACS Appl. Mater. Interfaces* **2016**, *8*, 3258–3267.
[51] Y. Zhao, Y. Zhang, K. Z. Xu, *Int. J. Electrochem. Sci.* **2019**, *14*, 3885–3896.
[52] S. Liu, D. Ni, H. F. Li, K. N. Hui, C. Y. Ouyang, S. C. Jun, *J. Mater. Chem. A* **2018**, *6*, 10674–10685.
[53] B. S. Singu, R. Kuchi, P. C. Van, D. Kim, K. R. Yoon, J. R. Jeong, *ChemNanoMat* **2019**, *5*, 1398–1407.
[54] Y. Wang, D. Yang, J. Lian, J. Pan, T. Wei, Y. Sun, *J. Alloys Compd.* **2017**, *735*, 204–652.
[55] A. T. A. Ahmed, B. Hou, H. S. Chavan, Y. Jo, S. Cho, J. Kim, S. M. Pawar, S. Cha, A. I. Inamdar, H. Kim, H. Im, *Small* **2018**, *14*, 1800742.

Manuscript received: January 26, 2022
Revised manuscript received: April 10, 2022
Accepted manuscript online: April 23, 2022